A tool development of rigorous Schrödinger/Luttinger based Monte Carlo codes for scaled MOS studies in terms of crystal orientation, channel direction, mechanical stress and applied voltage

Takako Okada
Corporate Research & Development Center
Toshiba Corporation
Kawasaki 212-8582, Japan
E-mail:t-okada@amc.toshiba.co.jp

***Abstract*— In order to study scaled devices in the 40nm regime and beyond, it is necessary to use rigorously theoretical and physical-based TCAD tools instead of empirically or phenomenologically calibrated approaches, otherwise full development and understanding of the devices will be retarded. In view of this situation, the author has developed a prototype rigorous Schrödinger/Luttinger based Monte Carlo tool for scaled MOS device designing in terms of crystal orientation, channel direction, mechanical stress and applied voltage, while also emphasizing flexibility for device modification and reliable prediction. In this paper, detailed mathematical derivations are presented and distinctive p-channel MOS inversion characteristics for Si, SiGe, and Ge are demonstrated. Moreover, experimental results for model verifications are presented.**

Keywords; Schrodinger equation; Luttinger Hamiltonian; MOS hole transport

I. INTRODUCTION

The design of scaled devices has been the subject of a great deal of research and discussion, for instance, on how to reduce the mobility imbalance in scaled strained p- and n-channel devices, how to control Ge concentration in Si to optimize the performance of bipolar devices, and how to improve mobility characteristics in high-K gate stacked. Having focused on the basic physics without pursuing any empirical or phenomenological approaches, the author has developed the prototype of a rigorous Schrödinger/Luttinger based Monte Carlo tool for the study of scaled MOS devices in terms of crystal orientation, channel direction, mechanical stress and applied voltage, while also emphasizing flexibility for device modification and reliable prediction. This paper pays particular attention to p-channel parts in CMOS because of current pressing needs of industry. This paper presents (1) basic algorithm of rigorous Schrödinger/Luttinger based Monte Carlo, (2) typical simulated results of p-channel MOS inversion layers, (3) scattering rates characteristic of bulk and inversion layer, (4) typical results of SiGe MOS characteristics, and (5) experimental results for model verifications.

The author also presents individual outputs with special visual aids to facilitate discussion.

II. BASIC ALGORITHM AND CODE DEVELOPMENT

The rigorous Schrödinger/Luttinger[1,2] based prototype codes are composed of (1)Monte Carlo parts with anisotropic subband energy and scattering rates[3-5], (2)extended Luttinger equations with stress/strain tensor and matrix solvers, and (3)Poisson solver. Figure 1 shows a schematic illustration of hole subbands in inversion layer and scattering processes of intra- and inter-subband in Monte Carlo part. In the prototype code, optical phonon scattering process and acoustic phonon process are considered. Figure 2 shows a whole flow chart of Schrödinger/Luttinger codes. From the Schrödinger/Luttinger part, subband structures and wave functions are output. Using these values, scattering rates are rigorously calculated. Finally, semi-classical hole Monte Carlo calculation is performed with the subband structures and the scattering rates.

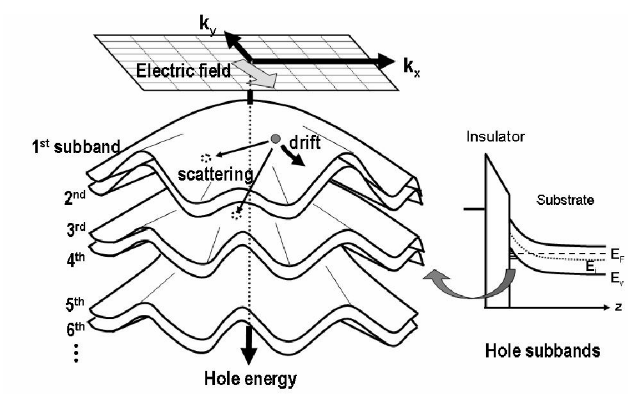

Figure 1. Schematic illustration of hole subbands in inversion layer and scattering processes of intra- and inter-subband in Monte Carlo part.

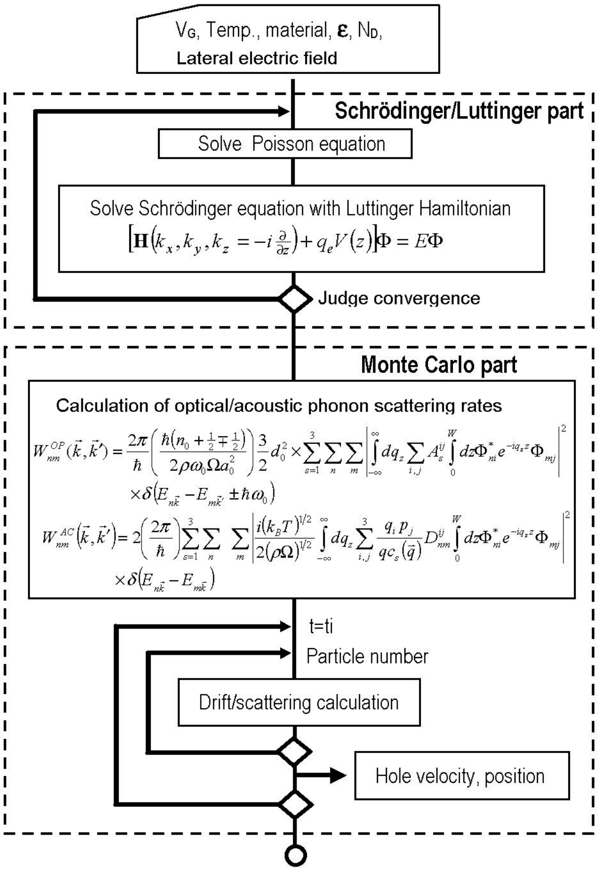

Figure 2. Flow chart of Schrödinger/Luttinger Monte Carlo codes. $V(z)$ is a potential, z depth, Φ wave function, and q_e electron charge. W^{OP} and W^{AC} are scattering rates with optical phonon process and acoustic phonon process, respectively. Indices n and m denote a subband number. A^{ij} and D^{ij} are deformation potential operators. Other notations are in [4] and [5].

Luttinger Hamiltonian for various orientations was derived mathematically from a general 6x6 k· p Hamiltonian for diamond lattice[6,7]. After rotating a coordination system for the original k· p Hamiltonian to accord the z direction with surface orientation, unitary transformation corresponding to envelope- functions in Luttinger's procedure was performed. The Schrödinger equation was solved as an eigenvalue equation derived from a finite difference discretization of 6x6 Luttinger Hamiltonian matrix.

The most important feature of the prototype code is rigorous treatment of phonon scattering rates. Madarasz-Szmulowicz model[4] and Szmulowicz model[5] are adopted for acoustic phonon scattering and optical phonon scattering, respectively. Both scattering rate per unit time at each energy state and its angular distribution are kept during the Monte Carlo calculation. Post-scattering state is selected by following the angular distribution with random number. However, one of the numerical difficulties is the enormous calculation time required in the scattering rate calculation, since large eigenvalue equation has to be solved at each energy state and along each direction an enormous number of times. In order to reduce the load, bicubic spline interpolation is applied carefully using $W(\boldsymbol{k},\boldsymbol{k}')$ values for fixed $\boldsymbol{k}'$ point calculated in advance.

III. Typical Output Results

Typical output results of hole subband energy in silicon inversion layer for various kinds of surface orientations and stress conditions are shown in Fig.3. It should be noted that distinctive subband structures were calculated among (110), (111), (112), and (100) surfaces. For the (001) surface, the summit of the subband is gentle, and eight ridges of the subband continue to <110> directions with gradual slope and <100> directions with somewhat steep slope. On the other hand, it should be noted that the summit of the (110) surface is markedly acute at Γ point, and six ridges continue to <-110> directions and <-112> with steep slopes. The subband for (111) surface is nearly isotropic and no ridge appears. For the (112) surface, sharp ridges along [11-1] and [-110] are calculated. These features affect characteristics of hole drift mobility for each surfaces, especially its anisotropy for channel directions.

Moreover, Fig. 3 indicates that stresses vary subband structures markedly. In case of (001) surface, intensive uniaxial compressive stress along [110] direction extinguishes particular ridges along [110] direction and [-1-10] virtually. The transformation brings about remarkable anisotropy of hole drift velocity. For the (110) surface, [-110] ridge almost disappears and the summit at Γ point becomes steeper by uniaxial compression along [-110] direction. The stress is expected to gain hole drift velocity for all directions.

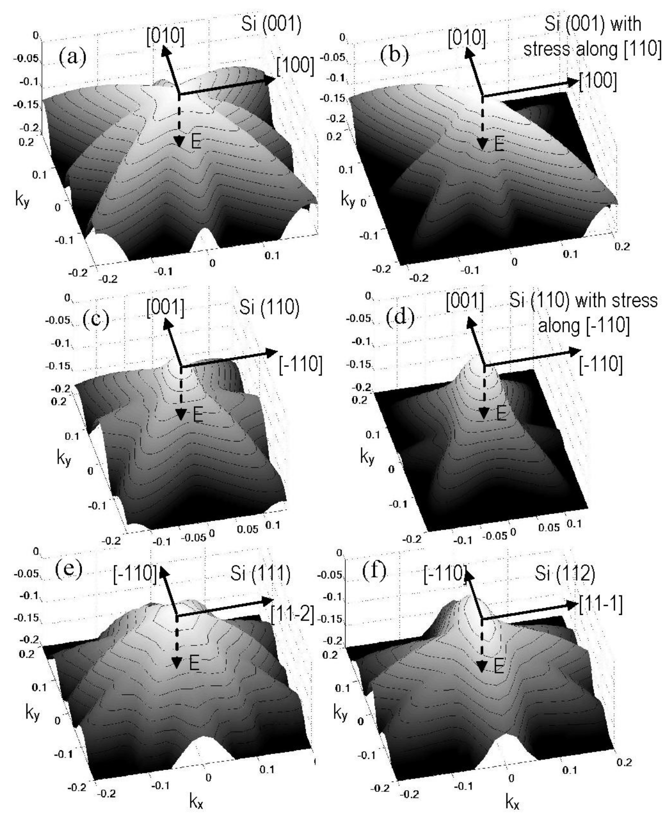

Figure 3. Typical output results of contour energy surfaces of lowest subbands in hole inversion layers for various orientations. Compression of 1GPa is applied in (b) and (d). Energy was measured from Γ point. Interval of contours is 20meV. Units of k_x and k_y are $2\pi/a_0$.

Typical scattering rate characteristics of hole inversion layer, namely, calculation results for Si (110) surface, are shown in Fig. 4. The indices 1-6 designate a subband number counted from the lowest subband. "1→1,2" denotes the sum of scattering processes from the first subband to the first and the first to the second. Silicon subbands are composed of many paired subbands which are quantized each other but similarly same as shown schematically in Fig.1. Figure 4 shows scattering rates from the first subband to each paired subbands. In the previous work on p-bulk[8], it was reported that the major part of the scattering process of p-bulk was intraband scattering of heavy hole, and interband scattering rate was only approximately 10 % of the total rate. Consequently, heavy hole occupied more than 85 % in hole transport of p-bulk. On the other hand, it is revealed from Fig. 4 that the intraband scattering rate accounts for nearly half of the total rate and the ratio of interband scattering is comparable to that of intraband scattering. Therefore, the occupation ratios for the third subband and the upper subbands become large relative to bulk. In the case of Si (110), the occupation ratios calculated from Monte Carlo part were ≈70 % for the sum of the first and the second, ≈20 % for the sum of the third and the fourth, and ≈10 % for the sum of the fifth and the sixth.

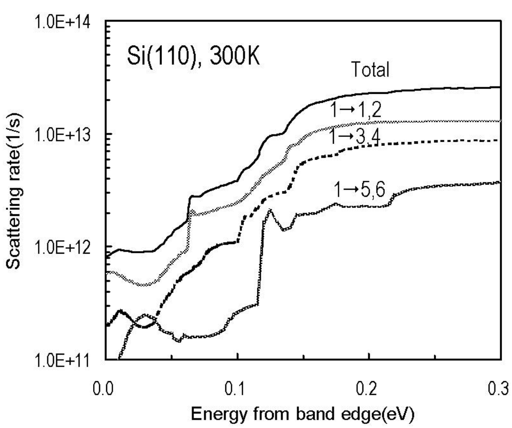

Figure 4. Scattering rate characteristics of the lowest subband of Si (110) surface. The indices 1-6 denote a subband number.

Figure 5(a) shows a typical result of an angular distribution of scattering rate for Si (110) surface. In Fig. 5(a), incident direction is set as the $\boldsymbol{k}_i$ direction, x-axis is [-110] direction, and y-axis is [001]. Length from the origin indicates the scattering rate at the direction. It should be noted that a markedly anisotropic distribution appears both for the optical phonon scattering and for the acoustic phonon scattering corresponding to the anisotropic structure of subband shape shown in Fig. 3(c). However, symmetric properties are different between optical phonon and acoustic phonon, since the optical branch for silicon is assumed to be dispersionless while the acoustic branch is calculated with polarization vectors given by Ehrenreich and Overhauser[9] as described by equations inserted in Fig. 2. It is revealed that backward scattering for incident direction is dominant in the acoustic phonon scattering process. Figure 5(b) shows a resulting hole distribution in 2D momentum space. Affected directly by the anisotropy of scattering rates, hole also distributes around the ridge of the subband shown in Fig. 3(c). Therefore, curvature around the ridge influences the hole mobility.

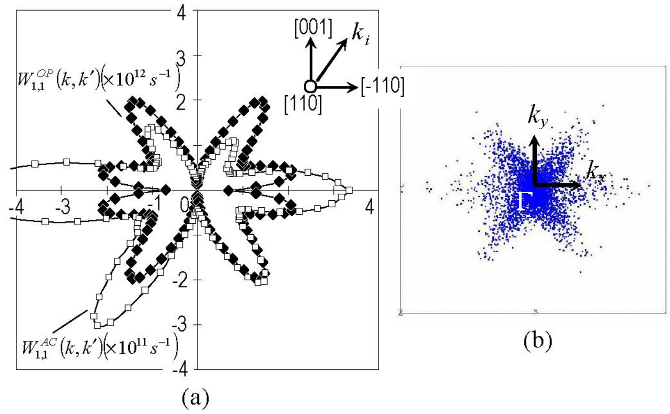

Figure 5. Angular distribution of intraband scattering rate of lowest subband of Si (110) surface at 300 K is plotted in (a). Acoustic scattering is the value at an enrgy of 100 meV and phonon scattering is at 150 meV. A corresponding hole distribution in momentum space is plotted in (b). Lateral electric field is set as 5kV/cm along [-110].

Figure 6 shows typical results of phonon-limited hole mobility for various channel directions and various stresses on Si (110) under the condition that gate voltage is -0.65 V, oxide thickness is 1 nm, and lateral electric field is 5 kV/cm. Uniaxial stress is applied along [-110] or [001] direction. The hole mobility is calculated by dividing the averaged hole velocity at steady state by the lateral electric field. For unstrained Si (110), the hole mobility along [-110] direction is calculated to be 27 % larger than the value along [001]. It should be noted that the hole mobility under uniaxial 1 GPa compression along [-110] is twice that of the hole mobility for unstrained surface. This is mainly because the curvature of subband energy surface becomes abrupt due to the stress as shown in Fig. 3(d). Moreover, it should be noted that uniaxial tension along [001] increases greatly due to the hole mobility for all channel directions as well as the [-110] compression. Effects of [-110] tension and [001] compression on the hole mobility are relatively small.

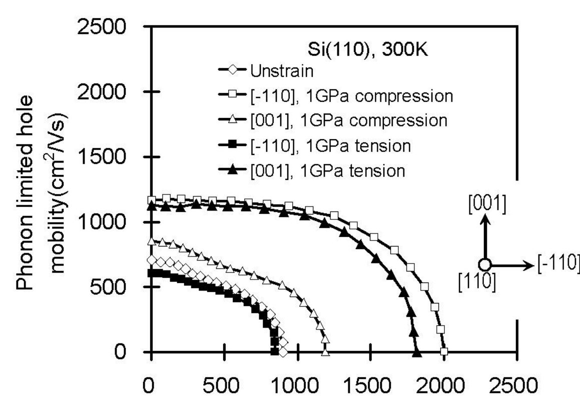

Figure 6. Phonon-limited hole mobility on Si (110) surface as functions of channel direction and stress condition. Stress is uniaxial along the direction described in legend.

As a last output example, germanium and $Si_{1-x}Ge_x$ characteristics in terms of strain and composition are shown in Fig. 7. Hole effective mass of the lowest subband is plotted as functions of biaxial stress and material composition as an indicator of transport performance. It can be seen that distinctive variation can be obtained. In particular, it has been found that hole effective mass in Ge decreases remarkably in the case of biaxial compression and increases in the case of biaxial tension. This is because subband structure around Γ point becomes remarkably acute and ridges on the subband surface become sharp under the biaxial compression as shown in Figs. 7(b) and (c). In other words, hole mobility in Ge has been predicted to increase under biaxial compression contrary to the Si case. Similar dependence on the stress field has been predicted for $Si_{1-x}Ge_x$ including high content Ge.

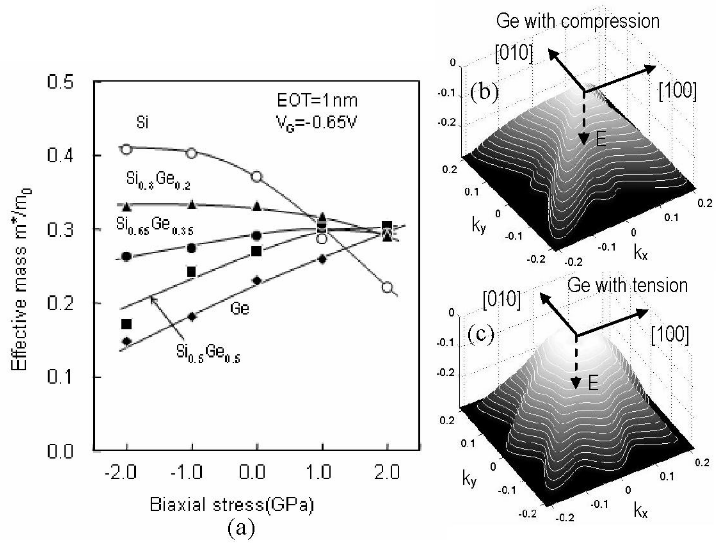

Figure 7. $Si_{1-x}Ge_x$ characteristics in terms of composition and biaxial stress are plotted in (a). Surface orientation is set as (001). Contour plot of hole lowest subband of (001) Ge at V_G= -0.65V under 2GPa biaxial compression is shown in (b) and under 2GPa tension is shown in (c), respectively. Energy was measured from Γ point. Interval of contours is 20meV. Units of k_x and k_y are $2\pi/a_0$.

IV. EXPERIMETAL VERIFICATIONS

In order to verify the codes, MOS cantilever experimentations have been conducted as shown in Fig. 8. Drain currents were measured upon applications of external uniaxial stress. The amounts of additional strain $\Delta\varepsilon_{ij}$ were calculated by the following equation,

$$\Delta\varepsilon_{ij} = (3Z \times b \times \Delta h)/L^3,$$

where Δh, Z and L are indicated in the figure and b is a half of the wafer thickness. Δh was measured using a micrometer head. In case of [110] Si p-channel on (100) Si, drain current gain has been measured decrease with compressive strain $\Delta\varepsilon_{ij}$ drain in the pentode region contrarily to the triode region, which is consistent with the simulated results.

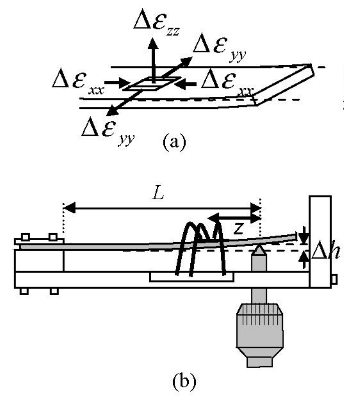

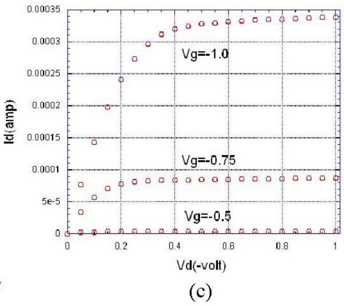

	Gain
Triode	44.28 at Vd=-50mv
Pentode	22.96 at Vd=-1.0V

(d)

Figure 8. MOS cantilever experimental setup. (a)MOS device on a beam chip, (b)sample holder and micro meter head, and (c)(d) experimental results. Dimensions of the specimen are as follows: L=39.08mm, Z=9.60mm and 2b=0.70mm. S/D is located on transversal to the beam, and generated strain is compressive around 10^{-5} to 10^{-4} on the S/D direction.

V. SUMMARY

Schrödinger/Luttinger based approach to the issue of scaled MOS transport was first applied for various crystal orientations, channel directions, applied voltages and mechanical stresses together with experimental verifications. Typical p-channel inversion characteristics for (110), (111), (112) and (001) surfaces were demonstrated. Moreover, effective mass characteristics were output as functions of germanium concentration. Details of mathematical derivations in Schrödinger/Luttinger part and scattering rate procedures have also been reported with calling upon current references.

[1] J. M. Luttinger and W. Kohn, "Motion of electrons and holes in perturbed periodic fields," Phys. Rev., vol. 97, no. 4, pp. 869-883, February 1955.

[2] S. Rodriguez, J. A. Lopez-Villanueva, I. Melchor and J. E. Carceller, "Hole confinement and energy subbands in silicon inversion layer using the effective mass theory," J. Appl. Phys., vol. 86, no. 1, pp.438-444, July 1999.

[3] M. Tiersten, "Acoustic-mode scattering of holes," IBM J. Res. Dev., vol. 5, pp. 122-131, 1961.

[4] F. L. Madarasz and F. Szmulowicz, "Transition rates for acoustic-phonon – hole scattering in p-type silicon with nonparabolic bands," Phys. Rev. B, vol. 24, no. 8, pp. 244611-244622, October 1981.

[5] F. Szmulowicz, "Calculation of optical- and acoustic- phonon–limited conductivity and Hall mobilities for p-type silicon and germanium," Phys. Rev. B, vol. 28, no.10, pp. 285943-285963, November 1983.

[6] J. E. Dijikstra and W. Th. Wenckebech, "Hole transport in strained Si," J. Appl. Phys., vol. 81, no. 3, pp. 1259-1263, 1997.

[7] J. M. Hinckley and J. Singh, "Hole transport theory in pseudomorphic $Si_{1-x}Ge_x$ alloys grown on Si (001) substrates," Phys. Rev. B, vol. 41, no. 5, pp. 412912-412926, February 1990-I.

[8] T. Okada and H. Yoshimura, "Rigorous mathematical calculation of p- and n-mobility as functions of mechanical stress, electric field, current direction and substrate indices for scaled CMOS designing," VLSI Symp., pp. 116-117, 2004.

[9] H. Ehrenreich and A. W. Overhauser, "Scattering of holes by phonons in germanium," Phys. Rev., vol. 104, no. 2, pp. 331-342, October 1956.